Materials Today Bio 38 (2026) 103269

Contents lists available at ScienceDirect

Materials Today Bio

journal homepage: www.journals.elsevier.com/materials-today-bio

Fluorinated charge-reversible phthalocyanine nanoemulsions for glioma-targeted dual-modal imaging and self-oxygenated phototherapy

Tingjuan Wu [a,1], Qiao Yu [a,1], Jing Zhang [c], Lijun Zhu [a], Chaohui Ye [a,b], Xin Zhou [a,b,*], Yu Li [a,b,**], Zhong-Xing Jiang [a,b,***]

[a] State Key Laboratory of Magnetic Resonance Spectroscopy and Imaging, National Center for Magnetic Resonance in Wuhan, Wuhan Institute of Physics and Mathematics, Innovation Academy for Precision Measurement Science and Technology, Chinese Academy of Sciences-Wuhan National Laboratory for Optoelectronics, Huazhong University of Science and Technology, Wuhan, 430071, China
[b] University of Chinese Academy of Sciences, Beijing, 100049, China
[c] School of Life Science and Engineering, Lanzhou University of Technology, Lanzhou, 730050, China

ARTICLE INFO

Keywords:
Amphiphilic phthalocyanine
Charge-reversible polymers
^{19}F MRI-NIRF dual imaging
Glioma phototherapy
Oxygen delivery

ABSTRACT

Gliomas are highly aggressive brain tumors with poor prognosis, limited by inadequate targeting, tumor hypoxia, and the restrictive blood-brain barrier (BBB). Here, we present a fluorinated phthalocyanine manganese-based nanoemulsion for dual-modal imaging and effective phototherapy of gliomas. The amphiphilic phthalocyanine, engineered through side-chain modification and Mn^{2+} chelation, exhibits "turn-on" near-infrared fluorescence (NIRF), sensitive fluorine-19 magnetic resonance imaging (^{19}F MRI), and high phototherapy efficacy. Self-assembly with fluorinated oil and coating with a folic acid-modified charge-reversible polymer produces a nanoemulsion with markedly enhanced imaging sensitivity and phototherapeutic efficacy. *In vitro* and *in vivo* studies demonstrate superior tumor targeting, deep penetration, efficient cellular uptake, dual-organelle localization, and induction of both apoptosis and pyroptosis. In orthotopic glioma models, the nanoemulsion crosses the BBB, accumulates in tumors, suppresses tumor growth, and prolongs survival without obvious systemic toxicity. This strategy underscores the promise of integrating photosensitizer engineering with smart nanoemulsion design for targeted, efficient, and imaging-guided cancer therapy.

1. Introduction

Gliomas are highly aggressive primary brain tumors with high mortality, frequent recurrence, and poor prognosis [1–3]. Standard treatments offer limited benefit, with a median survival of only 14-17 months [4,5]. Their invasive, angiogenic, and metastatic nature leads to unclear tumor margins and rapid relapse after treatment [6]. Treatment is further hindered by low specificity, severe side effects, hypoxia-induced drug resistance, and the protective BBB [7,8]. These challenges highlight the urgent need for improved imaging and more effective therapies [9–12].

Phototherapy [13–16], including photothermal therapy (PTT) and photodynamic therapy (PDT), offers a promising alternative to glioma chemotherapy by killing tumor cells through localized heat or reactive oxygen species (ROS) generated by photosensitizers while reducing systemic toxicity and drug resistance [17,18]. Many photosensitizers are also fluorescent, enabling real-time fluorescence imaging (FLI)-guided therapy [19]. However, conventional FLI suffers from limited light

* Corresponding author. State Key Laboratory of Magnetic Resonance Spectroscopy and Imaging, National Center for Magnetic Resonance in Wuhan, Wuhan Institute of Physics and Mathematics, Innovation Academy for Precision Measurement Science and Technology, Chinese Academy of Sciences-Wuhan National Laboratory for Optoelectronics, Huazhong University of Science and Technology, Wuhan, 430071, China.
** Corresponding author. State Key Laboratory of Magnetic Resonance Spectroscopy and Imaging, National Center for Magnetic Resonance in Wuhan, Wuhan Institute of Physics and Mathematics, Innovation Academy for Precision Measurement Science and Technology, Chinese Academy of Sciences-Wuhan National Laboratory for Optoelectronics, Huazhong University of Science and Technology, Wuhan, 430071, China.
*** Corresponding author. State Key Laboratory of Magnetic Resonance Spectroscopy and Imaging, National Center for Magnetic Resonance in Wuhan, Wuhan Institute of Physics and Mathematics, Innovation Academy for Precision Measurement Science and Technology, Chinese Academy of Sciences-Wuhan National Laboratory for Optoelectronics, Huazhong University of Science and Technology, Wuhan, 430071, China.
E-mail addresses: xinzhou@wipm.ac.cn (X. Zhou), liyu@wipm.ac.cn (Y. Li), zxjiang@apm.ac.cn (Z.-X. Jiang).
[1] T. Wu and Q. Yu contributed equally to this work.

https://doi.org/10.1016/j.mtbio.2026.103269
Received 13 February 2026; Received in revised form 29 April 2026; Accepted 21 May 2026
Available online 22 May 2026

penetration, and PDT efficacy in gliomas is often hindered by poor photosensitizer accumulation due to the blood-brain barrier (BBB) [20,21] and hypoxia in the tumor microenvironment (TME) [22,23]. Addressing these issues requires imaging modalities with deeper penetration and delivery systems that enhance photosensitizer accumulation and oxygen availability in tumors.

Near-infrared fluorescence imaging (NIRFI) offers deeper tissue penetration than conventional FLI [24–27], while fluorine-19 magnetic resonance imaging (^{19}F MRI) enables background-free, non-ionizing, and deep "hot spot" imaging [28–30]. Their combination allows sensitive, real-time, and quantitative monitoring of gliomas and the therapy [31–34]. Targeted delivery can be achieved by exploiting folate receptor α (FRα) overexpression in glioma cells for selective photosensitizer uptake [35,36]. Acid-responsive, charge-reversible nanoparticles further improve tumor specificity by enhancing uptake in acidic TME and reducing off-target effects [37–39]. Fluorinated compounds used in ^{19}F MRI are well known for their ability to carry oxygen, thereby alleviating hypoxia and enhancing the efficacy of PDT [40–44]. Integrating these strategies into a single theranostic nanoplatform could address major challenges in glioma imaging and therapy.

Phthalocyanine is a potent photosensitizer with high photostability, strong NIR absorption/emission, and tunable properties via metal chelation [45,46]. However, its hydrophobic planar structure always leads to poor solubility, severe aggregation, fluorescence (FL) quenching, and reduced phototherapy efficacy under physiological conditions, limiting its clinical application [47]. Structure engineering, such as introducing fluorinated amphiphilic side-chains and metal chelation, can mitigate aggregation, activate FL, and simultaneously enable ^{19}F MRI and oxygen delivery. This approach produces effective dual-modal imaging and therapeutic agents for gliomas, although the structural modification of phthalocyanine remains a significant challenge.

Herein, we developed an "all-in-one" phthalocyanine nanoemulsion

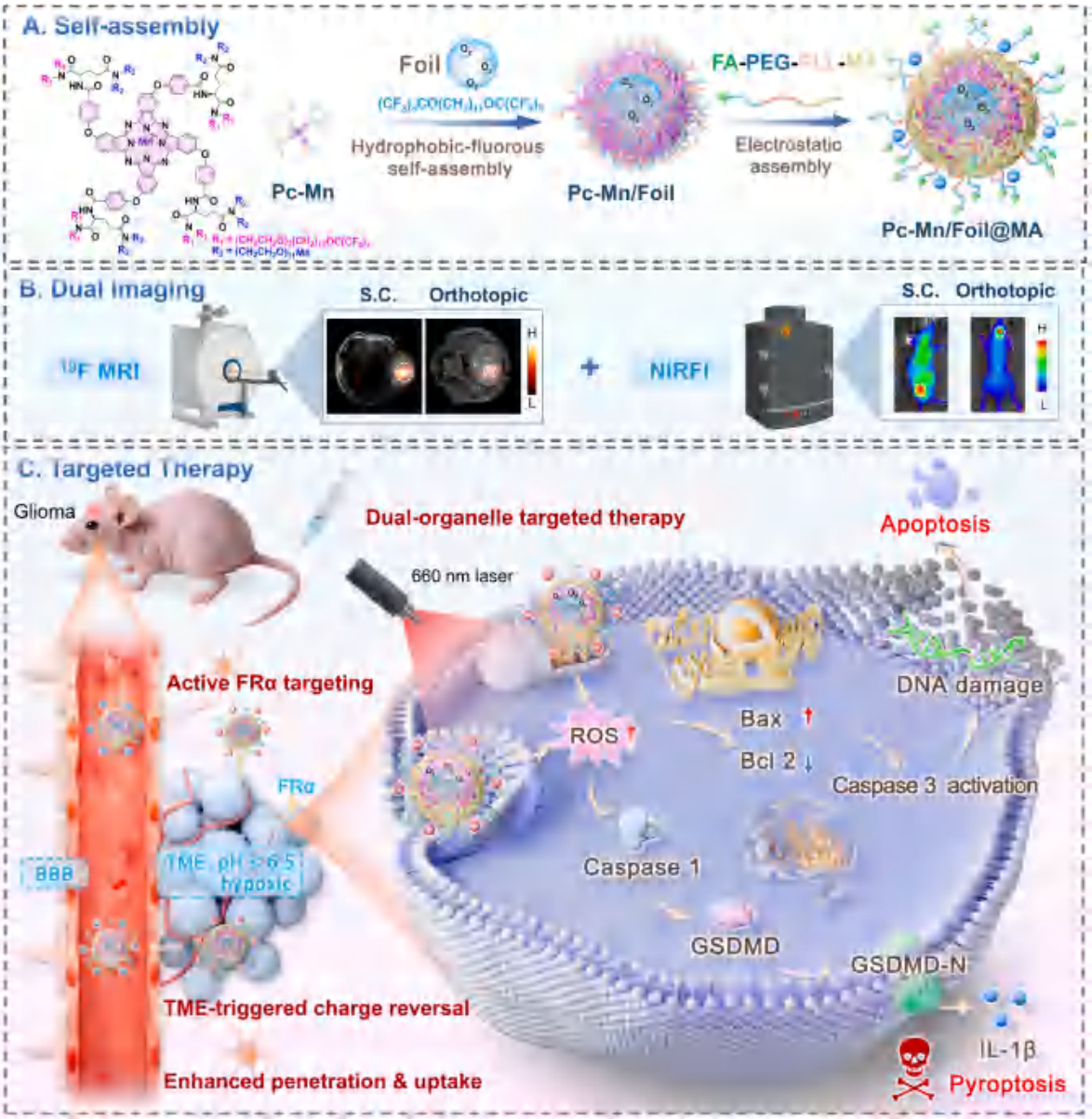

Scheme 1. Schematic illustration of phthalocyanine nanoemulsion for glioma imaging and phototherapy. Amphiphilic ***Pc*-Mn** co-assembles with **Foil** and is further coated with a folate-modified charge-reversible polymer (**FA-PEG-PLL-MA**) to yield ***Pc*-Mn/Foil@MA** (A). After intravenous injection, ***Pc*-Mn/Foil@MA** crosses the BBB and enables dual-modal ^{19}F MRI/NIRFI of gliomas via FRα-mediated targeting (B). In the acidic TME, charge reversal enhances penetration and dual-organelle (plasma membrane and mitochondria) targeted uptake. Upon irradiation, ***Pc*-Mn/Foil@MA** induces apoptosis and pyroptosis through self-oxygenated phototherapy (C).

(***Pc*-Mn/Foil@MA**) that integrates NIRFI/^{19}F MRI, folate receptor targeting, acid-triggered charge reversal, and self-oxygenated PDT for dual-modal imaging and phototherapy of both subcutaneous and orthotopic gliomas (Scheme 1). First, phthalocyanine was modified with 16 monodisperse oligo(ethylene glycol) (M-OEG) chains, 8 perfluoro-*tert*-butoxy (PFTB) groups, and Mn^{2+} chelation to afford amphiphilic ***Pc*-Mn**, in which Mn^{2+} modulates the electronic structure and enhances ^{19}F MRI performance via paramagnetic relaxation effects. The ***Pc*-Mn** with excellent solubility contained 72 equivalent fluorine atoms and exhibited shortened ^{19}F relaxation times, which resulted in a strong ^{19}F MRI signal and activated NIRFI. To boost imaging, deliver oxygen, and enhance PDT efficacy [48,49], ***Pc*-Mn** was co-assembled with a PFTB-rich oil (**Foil**) [33] into a carrier-minimized nanoemulsion, where ***Pc*-Mn** acted as a macromolecular surfactant. Furthermore, coating with an acid-responsive, folic-acid-conjugated charge-reversal polymer (**FA-PEG-PLL-MA**) enabled selective targeting of FRα-overexpressing glioma cells. This design allows the nanoemulsion to maintain prolonged circulation under physiological conditions. Following endocytic uptake, acidic lysosomal compartments triggered charge reversal, promoting lysosomal escape and intracellular trafficking, thereby facilitating transcytosis-mediated BBB-associated transport. This nanoplatform provides a strategy for glioma imaging and therapy through combining improved photosensitizer performance, targeted delivery, and self-oxygenated phototherapy.

2. Results and discussion

2.1. Synthesis and characterization of phthalocyanine-manganese (Pc-Mn)

To optimize the physicochemical properties, two fluorinated amphiphilic phthalocyanines (***Pc*-1** and ***Pc*-2**) were synthesized, with ***Pc*-2** bearing twice the number of M-OEG and PFTB groups (Fig. 1A). Using a glutamic acid scaffold, a modular synthesis afforded multi-hundred-milligram quantities of ***Pc*-1** and ***Pc*-2** with an overall yield of >18% (Scheme S1), which were fully characterized by ^{1}H/^{13}C/^{19}F NMR and HRMS (Supporting Information).

As designed, both ***Pc*-1** and ***Pc*-2** produced a sharp singlet ^{19}F NMR

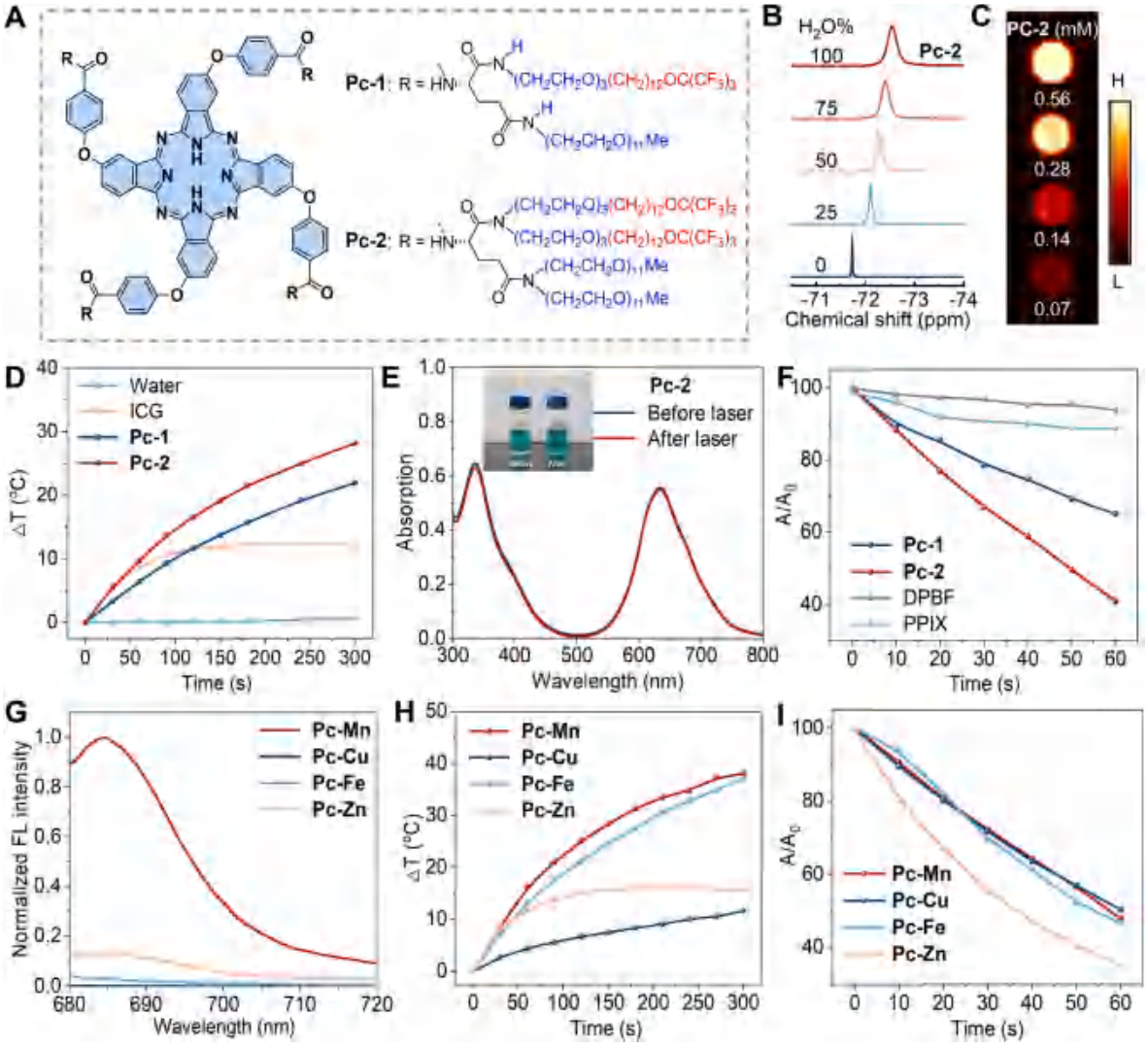

Fig. 1. Characterization of amphiphilic phthalocyanines and their chelates. Chemical structures of ***Pc*-1** and ***Pc*-2** (A). Partial ^{19}F NMR spectra (B, 10 μM in methanol-water) and ^{19}F MRI (C, 10 μM in methanol) of ***Pc*-2**. Irradiation time-dependent temperature increases (D, 10 μM) of ***Pc*-1** and ***Pc*-2**. Color and absorption spectra of ***Pc*-2** upon irradiation (E). Irradiation time-dependent absorption decay of DPBF (60 μM) in the presence of ***Pc*-1** and ***Pc*-2** (F, 1 μM). Normalized FL emission spectra (G), and irradiation time-dependent temperature increases (H, 20 μM) of ***Pc*-2** chelates. Irradiation time-dependent maximum absorption decay of DPBF (60 μM) in the presence of ***Pc*-2** chelates (I, 1 μM). A 660 nm laser was used in all cases with 1 W cm^{-2} for D, E, H, and 0.35 W cm^{-2} for F and I. The corresponding figures for ***Pc*-1** can be found in the Supporting Information. (For interpretation of the references to color in this figure legend, the reader is referred to the Web version of this article.)

peak at −71.8 ppm from all fluorine atoms (Fig. 1B; Fig. S1A), enabling sensitive ^{19}F MRI detection down to 0.14 mM (***Pc*-1**) and 0.07 mM (***Pc*-2**) with signal-to-noise ratios (SNRs) of 2.55 and 2.44, respectively (Fig. 1C; Fig. S1B). A linear LogSI (signal intensity) and LogC(^{19}F) correlation supported their quantitative ^{19}F MRI potential (Fig. S1C). Although the multiple M-OEG chains provided high water solubility, switching to an aqueous medium resulted in peak broadening and upfield shifts in the ^{19}F NMR due to aggregation (Fig. 1B; Fig. S1A). UV-Vis spectra revealed blue-shifted and weakened absorption in water, confirming aggregation (Fig. S2A). ***Pc*-2** exhibited tenfold stronger NIRF than ***Pc*-1** in methanol (Fig. S2B), likely due to reduced aggregation-caused quenching (ACQ) by the steric hindrance of the doubled M-OEG and PFTB groups. However, their FL was low in water. LogP and critical micelle concentration (CMC) measurements showed high hydrophilicity (LogP: 0.38 for ***Pc*-1**, -0.15 for ***Pc*-2**) (Fig. S2C) and strong self-assembly tendencies (CMC: 5.5 μM for ***Pc*-1**, 3.9 μM for ***Pc*-2**) (Fig. S2D and E), indicating the high aggregation tendency of the large hydrophobic aromatic core despite the presence of hydrophilic side-chains.

Upon laser irradiation, ***Pc*-1** and ***Pc*-2** produced temperature increases of 21 °C and 27 °C, respectively, outperforming clinically used ICG which only reached a 12 °C increase. (Fig. 1D; Fig. S3A and B–). Unlike ICG, which suffers from photobleaching, both showed excellent photostability over four irradiation-cooling cycles with no color or absorption changes (Fig. 1E; Fig. S3C–F). Using DPBF as a probe, ***Pc*-2** generated more $^1O_2$ than ***Pc*-1** and PPIX, the active photosensitizer in clinically approved 5-aminolevulinic acid-based PDT, indicating superior PDT activity (Fig. 1F; Fig. S4).

Given its superior NIRF-^{19}F MRI sensitivity and robust PTT/PDT capabilities, ***Pc*-2** was chosen for metal-ion chelation to further enhance performance. Among Mn^{2+}, Cu^{2+}, Fe^{3+}, and Zn^{2+}, Mn^{2+} caused a 90 nm redshift in the Q-band absorption (Fig. S2F), triggered a pronounced "turn-on" NIR fluorescence with an approximately tenfold increase in emission intensity in water (Fig. 1G), and enhanced photothermal performance (Fig. 1H), with only a minor reduction in singlet oxygen generation (Fig. 1I; Fig. S4). This fluorescence enhancement may be attributed to Mn^{2+} coordination-induced modulation of the electronic structure and aggregation behavior of the phthalocyanine core, which suppresses ACQ and reduces non-radiative decay pathways in aqueous media.

2.2. Formulation and characterization of nanoemulsion (Pc-Mn/Foil@MA)

The amphiphilic of ***Pc*-Mn** acts as a macromolecular surfactant, spontaneously co-assembling with **Foil** into stable carrier-minimized nanoemulsions (***Pc*-Mn/Foil**) without extra surfactant (Fig. 2A). To introduce TME-responsiveness and folate targeting, the charge-reversible polymer (**FA-PEG-PLL-MA**) and non-reversible control (**FA-PEG-PLL-SA**) were synthesized on a multi-hundred-milligram scale and confirmed by ^{1}H NMR (Supporting Information) [37–39]. **FA-PEG-PLL-MA** exhibited rapid charge reversal at pH 6.0, shifting surface potential from −15 mV to +2 mV within 1 h, while **FA-PEG-PLL-SA** remained unchanged (Fig. 2B; Fig. S5A). The nanoemulsions were then coated with the polymers to yield ***Pc*-Mn/Foil@MA** and ***Pc*-Mn/Foil@SA** as a control.

Dynamic light scattering (DLS) showed ***Pc*-Mn/Foil@MA** had a hydrodynamic diameter of ~100 nm with a reduced polydispersity index (PDI) of 0.19 compared to ***Pc*-Mn/Foil** (PDI = 0.28) (Fig. 2C; Fig. S5B). Transmission electron microscopy (TEM) confirmed spherical morphology (Fig. 2C; Fig. S5C). To further evaluate colloidal stability under physiologically relevant conditions, the particle size and zeta potential were monitored over 72 h in phosphate-buffered saline (PBS) and Dulbecco's Modified Eagle Medium (DMEM) containing 10% fetal bovine serum (FBS). The hydrodynamic size showed a slight increase over time, while no significant aggregation or precipitation was observed. Meanwhile, the zeta potential remained negative without charge reversal. These results indicate good stability in biologically relevant environments (Fig. S5E and F).

Encapsulation of ***Pc*-Mn**, **Foil**, and **FA-PEG-PLL-MA** was verified by elemental mapping, UV-Vis and FL spectra (Fig. 2D–F). At pH 6.0, ***Pc*-Mn/Foil@MA** showed a surface charge shift from −20 mV to +19 mV after 3 h, while ***Pc*-Mn/Foil@SA** remained unchanged (Fig. 2G; Fig. S5D), demonstrating charge-reversal behavior under acidic TME conditions.

Upon laser irradiation, both ***Pc*-Mn/Foil@MA** and ***Pc*-Mn/Foil@SA** increased the temperature by ~30 °C, corresponding to a high photothermal conversion efficiency (PCE) of 74% (Fig. 2H; Fig. S6). DPBF degradation under irradiation confirmed rapid ROS generation within 60 s (Fig. 2I), further verified by electron paramagnetic resonance (EPR) spectroscopy with TEMP as a spin trap, revealing characteristic signals of singlet oxygen ($^1O_2$) (Fig. 2J). Notably, compared with free ***Pc*-Mn**, the nanoemulsions ***Pc*-Mn/Foil**, ***Pc*-Mn/Foil@MA**, and ***Pc*-Mn/Foil@SA** exhibited enhanced $^1O_2$ generation under identical irradiation conditions, as evidenced by Singlet Oxygen Sensor Green (SOSG) fluorescence measurements (Fig. S4L). This enhancement is likely associated with the incorporation of **Foil**, which can serve as an oxygen reservoir [33,50]. Owing to its high oxygen solubility, the **Foil** core helps maintain oxygen availability during irradiation, leading to enhanced ROS generation.

Due to the shared PFTB structure in ***Pc*-Mn** and **Foil**, ***Pc*-Mn/Foil@MA** exhibited a single intense ^{19}F NMR peak at −71.8 ppm (Fig. 2K), which minimizes spectral artifacts and improves ^{19}F MRI sensitivity. It was detectable by ^{19}F MRI at 5 mM ^{19}F with an SNR of 5.3 in 614 s (Fig. 2L). In contrast, **Pc/Foil@MA** (without Mn^{2+}) required 10 mM ^{19}F for similar SNR, reflecting ***Pc*-Mn/Foil@MA**'s twofold higher sensitivity. Shorter T_1 (524 ms) and T_2 (170 ms) relaxation times in ***Pc*-Mn/Foil@MA** versus **Pc/Foil@MA** (T_1 = 756 ms, T_2 = 383 ms) confirmed signal enhancement by paramagnetic Mn^{2+}, which accelerates ^{19}F relaxation through enhanced local magnetic field fluctuations (Fig. S7). Additionally, the **Foil** component boosted the detection of ***Pc*-Mn** by ^{19}F MRI to 5 μM. Both **Pc/Foil@MA** and ***Pc*-Mn/Foil@MA** showed linear LogSI-LogC(^{19}F) correlations, supporting quantitative imaging (Fig. 2M; Fig. S8). Therefore, the self-assembly of ***Pc*-Mn** and **Foil** and the coating with **FA-PEG-PLL-MA** facilitated ***Pc*-Mn/Foil@MA** with a uniform spherical core-shell structure, high phototherapy potency, and pH-responsive charge reversal, while Mn^{2+} chelation and ^{19}F signal unification enabled sensitive and quantifiable ^{19}F MRI, establishing it as a versatile and effective glioma theranostic nanoplatform.

2.3. Cellular uptake and cytotoxicity of Pc-Mn/Foil@MA

The cellular uptake of ***Pc*-Mn/Foil@MA** by human glioma U-87 MG cells was investigated using confocal laser scanning microscopy (CLSM). Significantly higher uptake was observed at pH 6.5 compared to pH 7.4 (Fig. 3A), indicating enhanced internalization via acid-triggered charge reversal. Subcellular colocalization analysis with MitoTracker Green (MTG) and the plasma membrane stain DiI revealed pH-dependent localization behaviors: mitochondrial localization dominated at pH 7.4 (Fig. 3B), whereas dual plasma membrane and mitochondrial localization was observed at pH 6.5 (Fig. 3C). This distinct intracellular distribution is consistent with different charge states under varying pH conditions. At pH 6.5, ***Pc*-Mn/Foil@MA** are positively charged in the extracellular environment, promoting enhanced electrostatic interaction with the cell membrane and facilitating efficient cellular uptake. In contrast, at pH 7.4, the nanoemulsions remain negatively charged extracellularly, resulting in reduced membrane binding and uptake via conventional endocytosis. Following internalization, lysosomal acidification triggers charge reversal, as supported by lysosomal escape experiments (Fig. S9), enabling cytoplasmic release and subsequent mitochondrial accumulation driven by the mitochondrial membrane potential. Dual-organelle targeting is advantageous for phototherapy, as both the plasma membrane and mitochondria are key regulators of cell

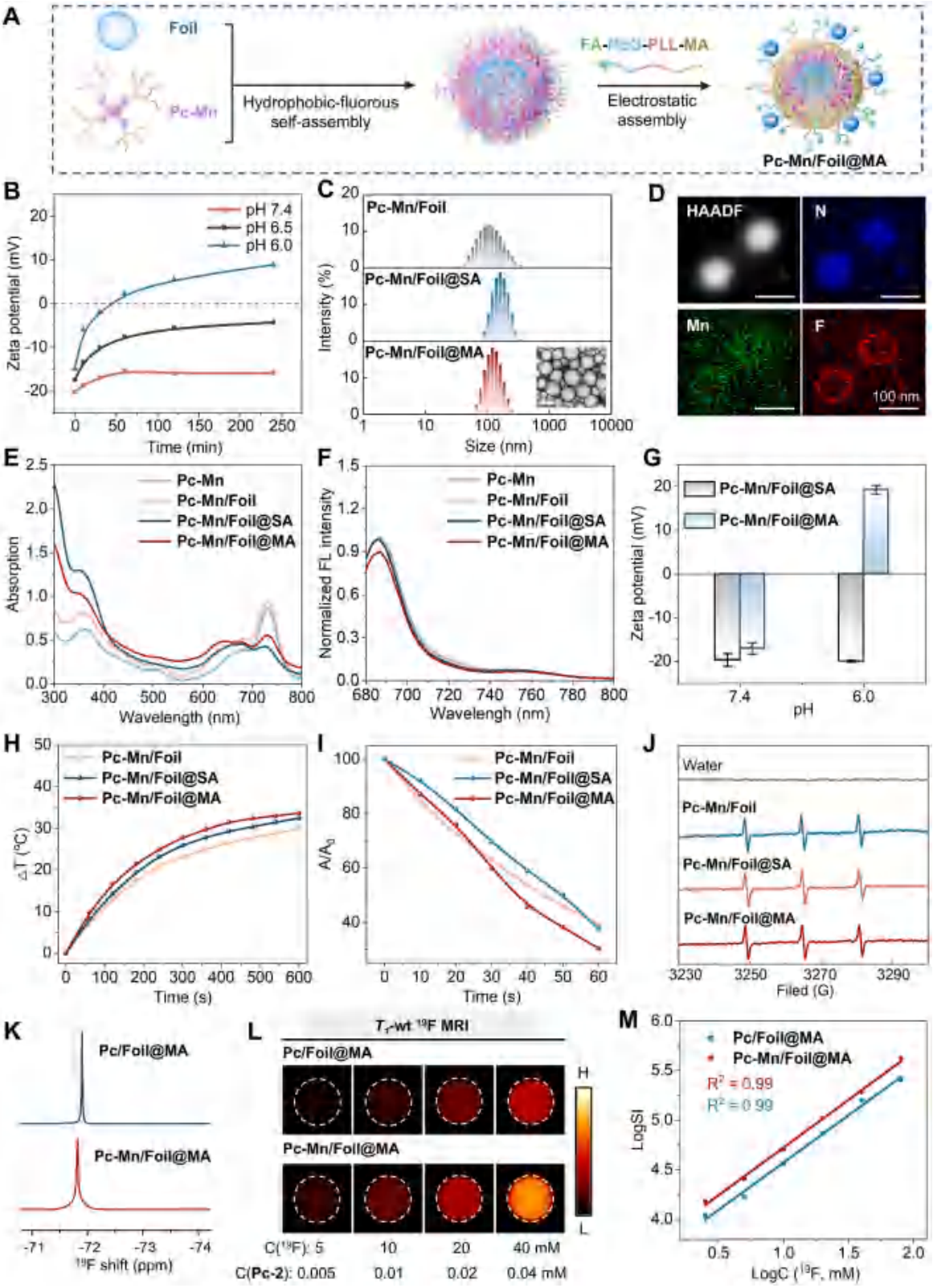

Fig. 2. Formulation and characterization of phthalocyanine nanoemulsions. Schematic illustration of the self-assembled nanoemulsion (A). pH-dependent surface charge changes of **FA-PEG-PLL-MA** (B). DLS with inserted TEM images of nanoemulsions (C, scale bar: 100 nm). Elemental mapping images of ***Pc*-Mn/Foil@MA** (D). Absorption spectra (E), normalized FL emission spectra (F), pH-dependent surface charge changes, n = 3 (G), and irradiation time-dependent temperature increases (H, 20 μM) of nanoemulsions. Irradiation time-dependent maximum absorption decay of DPBF (60 μM) in the presence of the nanoemulsions (I, 1 μM). EPR spectra of nanoemulsions after irradiation (J). Partial ^{19}F NMR spectra (K), T_1-weighted ^{19}F MRI (L) and plot of LogSI versus LogC(^{19}F) (M) of nanoemulsions. A 660 nm laser was used in all cases with 1 W cm^{-2} for H and 0.35 W cm^{-2} for I. Data are presented as mean ± SD; n = 3.

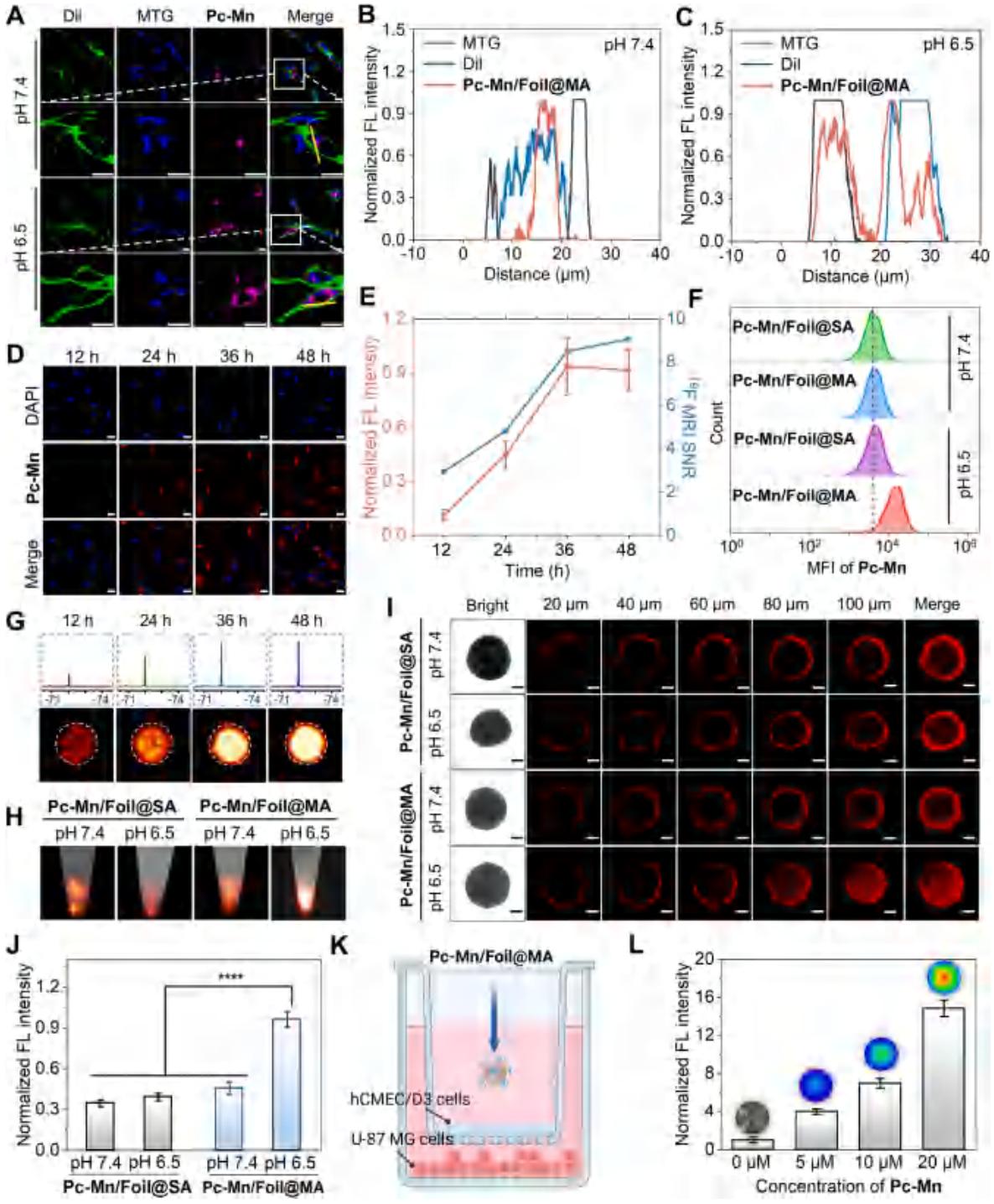

Fig. 3. Uptake of ***Pc*-Mn/Foil@MA** in U-87 MG cells and spheroids. CLSM images (A) and FL intensity profiles along the yellow lines (B: pH 7.4; C: pH 6.5) of ***Pc*-Mn/Foil@MA**-treated cells. Time-dependent CLSM images (D) and corresponding FL intensity (E, red) of ***Pc*-Mn/Foil@MA**-treated cells at pH 6.5. Flow cytometry analysis of nanoemulsion-treated cells (F). Time-dependent ^{19}F NMR and MRI of ***Pc*-Mn/Foil@MA**-treated cells (G) and plot of ^{19}F MRI SNRs (E, blue). ^{19}F MRI of nanoemulsion-treated cells (H). CLSM images (I) and FL intensity in the merge images (J) of nanoemulsion-treated spheroids. Schematic illustration of the transwell BBB model (K) and concentration-dependent FL intensity in the U-87 MG cells (L). Scale bar is 100 μm for I, and 20 μm for A, D. Data are presented as mean ± SD; n = 3, ****p < 0.0001. (For interpretation of the references to color in this figure legend, the reader is referred to the Web version of this article.)

death [51,52].

At pH 6.5, maximal uptake was observed at 36 h by time-dependent CLSM (Fig. 3D and E). Flow cytometry confirmed that ***Pc*-Mn/Foil@MA** showed high uptake at pH 6.5 but low uptake at pH 7.4, while ***Pc*-Mn/Foil@SA** exhibited low uptake under both conditions (Fig. 3F; Fig. S10A), supporting the critical role of acid-triggered charge reversal. Cellular uptake was further quantified by ^{19}F NMR and MRI. A ^{19}F NMR singlet was detected in lysates from cells treated with ***Pc*-Mn/Foil@MA** at pH 6.5, with corresponding MRI showing time-dependent signal increases consistent with CLSM data (Fig. 3E–G). ^{19}F MRI of 5×10^6 cells revealed stronger SNRs in ***Pc*-Mn/Foil@MA**-treated cells at pH 6.5 than at pH 7.4, whereas ***Pc*-Mn/Foil@SA** showed low SNRs under both conditions (Fig. 3H; Fig. S10B). These results confirm that acid-triggered charge reversal enhances cellular uptake, enabling targeted imaging and

therapy in acidic TME.

To evaluate folate-mediated uptake, a competitive inhibition assay was performed using excess free folic acid (FA). Pre-incubation with FA significantly reduced the cellular uptake of ***Pc*-Mn/Foil@MA** in a concentration-dependent manner, as confirmed by fluorescence quantification (Fig. S11), indicating a folate-associated internalization process. The cellular uptake mechanism was probed by altering temperature and inhibiting endocytic pathways. Compared with the control at 37 °C, FL was significantly diminished at 4 °C or in cells treated with genistein, an inhibitor of caveolin-mediated endocytosis (Fig. S12) [53]. These findings indicate that ***Pc*-Mn/Foil@MA** internalization is energy dependent and is mediated predominantly by caveolin.

To assess tumor penetration, 3D U-87 MG spheroids were used as *in vitro* tumor models. After 24 h incubation at pH 6.5, ***Pc*-Mn/Foil@MA** showed strong red FL throughout the spheroid (Fig. 3I), and quantitative analysis revealed that the FL intensity was twofold higher than in cells incubated at pH 7.4 or treated with ***Pc*-Mn/Foil@SA** (Fig. 3J), indicating charge reversal-promoted tumor penetration.

BBB penetration was evaluated using a transwell model with an hCMEC/D3 monolayer (Fig. 3K). The successful establishment of the *in vitro* BBB model was further confirmed by transendothelial electrical

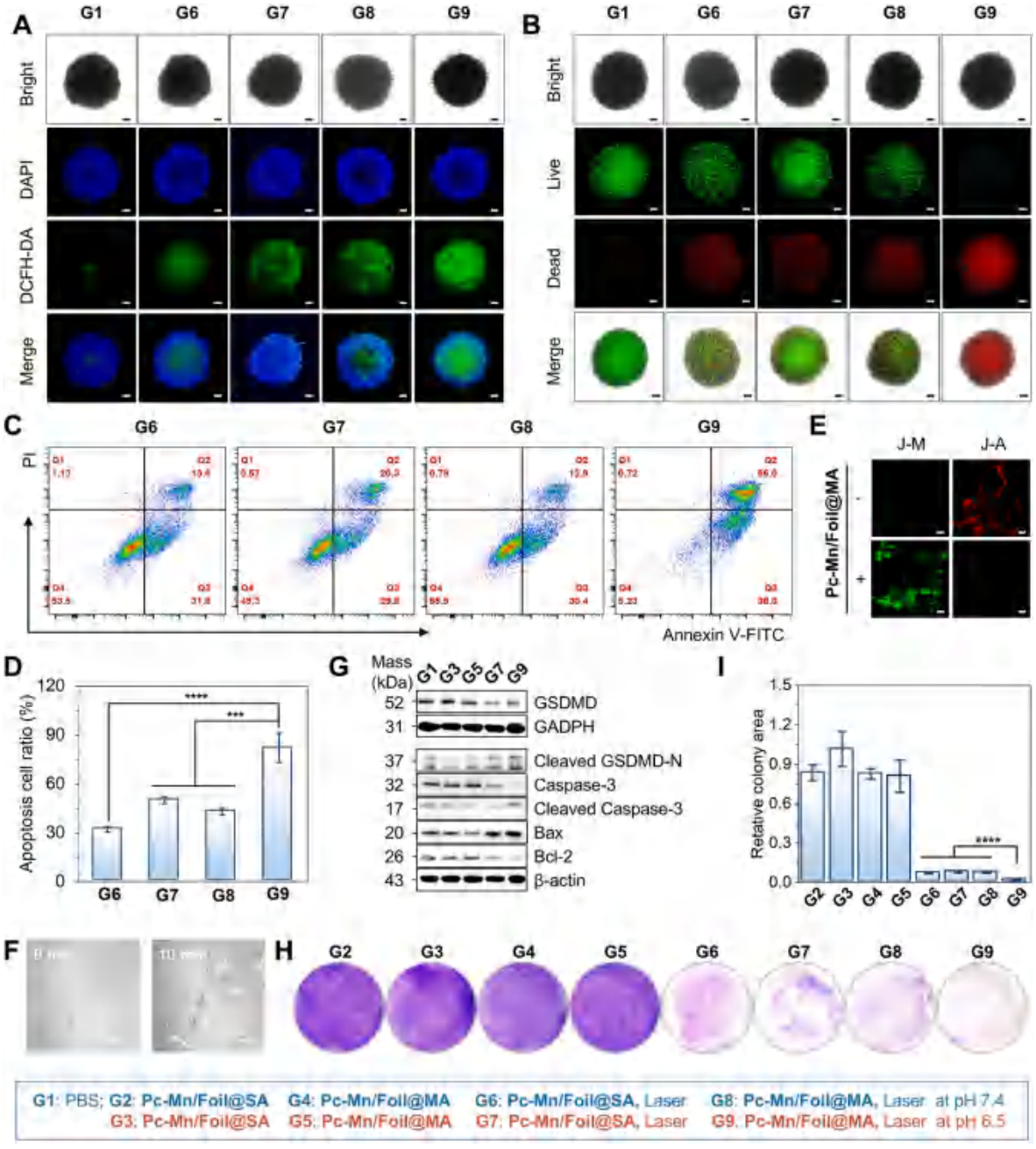

Fig. 4. Phototherapy efficacy of ***Pc*-Mn/Foil@MA** in U-87 MG cells and spheroids. CLSM images of DCFH-DA stained spheroids after the treatments (A). CLSM images of calcein-AM/PI double-stained spheroids after the treatments (B). Flow cytometry analysis (C) and corresponding apoptosis ratio (D) of treated cells. CLSM images of JC-1 stained cells after the treatments (E). Bright-field microscopy images (F) and Western blotting analysis (G) of ***Pc*-Mn/Foil@MA**-treated cells after irradiation. Representative crystal violet staining images of U87 cells (H) and quantitative assay of cell groups. A 660 nm laser at 0.35 W cm^{-2} was used in all cases. Scale bar: 20 μm. All concentrations refer to ***Pc*-Mn**. Data are presented as mean ± SD; n = 3, ***p < 0.001, ****p < 0.0001. (For interpretation of the references to color in this figure legend, the reader is referred to the Web version of this article.)

resistance (TEER) measurements, sodium fluorescein permeability, and apparent permeability coefficient (Papp) analysis, which collectively indicated the formation of a functionally restrictive endothelial barrier (Fig. S13). ***Pc*-Mn/Foil@MA** in the upper chamber crossed the monolayer and was uptaken by U-87 MG cells in the lower chamber, with FL intensity increasing in a concentration-dependent manner (Fig. 3L), demonstrating successful BBB transport.

The biocompatibility and photocytotoxicity of ***Pc*-Mn/Foil@MA** were evaluated in U-87 MG cells using the Cell Counting Kit-8 (CCK-8) assay. Without irradiation, both ***Pc*-Mn/Foil@MA** and ***Pc*-Mn/Foil@SA** showed excellent biocompatibility, maintaining >85% cell viability up to 40 μM at pH 6.5 and 7.4 (Fig. S14A and B). Hemolysis testing confirmed high blood compatibility, with <5% hemolysis at 100 μM (Fig. S14C). Upon 10 min of 660 nm laser irradiation (0.35 W cm^{-2}), significant photocytotoxicity was observed for ***Pc*-Mn/Foil@MA** at ~6 μM under pH 6.5, demonstrating enhanced photocytotoxicity via acid-triggered charge reversal (Fig. S14D).

ROS generation in 3D U-87 MG spheroids was visualized using DCFH-DA staining. Spheroids treated with ***Pc*-Mn/Foil@MA** and laser at pH 6.5 showed the strongest green FL (Fig. 4A; Fig. S14E). Live/dead staining further confirmed phototherapeutic efficacy with the highest dead-to-live cell ratio in ***Pc*-Mn/Foil@MA**-treated spheroids at pH 6.5 (Fig. 4B;, Fig. S14F). Lower ratios were observed at pH 7.4 and in ***Pc*-Mn/Foil@SA**-treated spheroids, highlighting the critical role of acid-triggered charge reversal in therapeutic efficacy.

Flow cytometry showed that the apoptosis rates induced by ***Pc*-Mn/Foil@MA** increased from 43% at pH 7.4 to 94% at pH 6.5 (Fig. 4C and D; Fig. S15), while ***Pc*-Mn/Foil@SA** caused minimal apoptosis under both conditions. Mechanistic studies revealed that ***Pc*-Mn/Foil@MA** induced mitochondrial dysfunction, as evidenced by a JC-1 red-to-green FL shift after irradiation (Fig. 4E). Bright-field microscopy revealed rapid plasma membrane blebbing and bubble formation within 10 min of irradiation (Fig. 4F; Fig. S16), characteristic of pyroptosis. Western blotting further confirmed activation of both apoptosis (upregulated cleaved caspase-3 and Bax, downregulated Bcl-2) and pyroptosis (cleaved GSDMD-N, Fig. 4G). A clonogenic assay demonstrated the long-term inhibition of glioma cell proliferation by ***Pc*-Mn/Foil@MA** at pH 6.5 with the smallest colony area and strongest growth suppression (Fig. 4H and I), indicating durable antitumor effects. Therefore, ***Pc*-Mn/Foil@MA** exhibited pH-dependent uptake via acid-triggered charge reversal, which targeted the plasma membrane and mitochondria, penetrated 3D spheroids, and crossed an *in vitro* BBB model, enabling strong ROS generation and potent phototherapy by inducing both apoptosis and pyroptosis.

2.4. *In vivo* biocompatibility and biodistribution of Pc-Mn/Foil@MA

The biocompatibility of ***Pc*-Mn/Foil@MA** was evaluated in female BALB/c nude mice via intravenous injection (15 μmol kg^{-1}), which showed no signs of acute toxicity over 7 days or organ abnormalities during gross necropsy. Inductively coupled plasma mass spectrometry (ICP-MS) analysis revealed a time-dependent clearance profile of Mn in both brain and major organs, with an initial increase after injection followed by a gradual decrease over time, and levels returning to baseline by day 21, indicating efficient systemic elimination and negligible long-term tissue retention (Fig. S17). In addition, histological analyses of major organs and brain tissue, including H&E staining of major organs as well as H&E and Nissl staining of brain tissue, showed no observable structural abnormalities or neuronal damage at day 21, further supporting the favorable *in vivo* biosafety profile of ***Pc*-Mn/Foil@MA** (Fig. S18). Whole-body NIRFI and ^{19}F MRI were conducted to assess biodistribution in U-87 MG subcutaneous tumor-bearing mice that received an intravenous injection of nanoemulsion at 2.5 μmol kg^{-1}. Time-dependent NIRFI showed widespread distribution of ***Pc*-Mn/Foil** and ***Pc*-Mn/Foil@SA**, with strong liver and lung signals, while ***Pc*-Mn/Foil@MA** exhibited predominantly tumor-localized FL and minimal off-target accumulation (Fig. 5A). Quantitative analysis revealed a steady increase in tumor FL intensity, which gradually plateaued after 36 h and remained high up to 72 h (Fig. 5B). The biodistribution was further confirmed by *ex vivo* NIRFI of major organs at 72 h post-injection (Fig. 5C). Quantitative analysis showed that ***Pc*-Mn/Foil** predominantly accumulated in the liver, while ***Pc*-Mn/Foil@SA** exhibited increased tumor uptake but still substantial hepatic distribution. In contrast, ***Pc*-Mn/Foil@MA** achieved the highest tumor accumulation (Fig. 5D), validating the synergistic role of acid-triggered charge reversal and folate targeting in enhancing tumor selectivity and reducing hepatic uptake.

Biodistribution was further evaluated in mice bearing orthotopic U-87 MG-Luc gliomas, with tumor formation confirmed via bioluminescence and ^{1}H MRI. After intravenous injection (2.5 μmol kg^{-1}), ***Pc*-Mn/Foil@MA**-treated mice showed strong brain region NIRFI signals colocalized with tumor bioluminescence, indicating effective targeting (Fig. 5E). The NIRFI signal at the tumor site increased continuously, slowed after 36 h, and remained relatively stable through 72 h (Fig. 5F). *Ex vivo* imaging of excised organs and brains at 72 h confirmed prominent accumulation of ***Pc*-Mn/Foil@MA** in orthotopic gliomas. In contrast, ***Pc*-Mn/Foil** and ***Pc*-Mn/Foil@SA** showed weaker tumor signals and more pronounced off-target distribution (Fig. 5G and H). In contrast, ***Pc*-Mn/Foil** and ***Pc*-Mn/Foil@SA** showed weaker tumor signals and higher off-target accumulation. NIRFI of brain slices and semi-quantitative analysis further demonstrated the superior BBB penetration and glioma targeting of ***Pc*-Mn/Foil@MA** (Fig. 5I and J). The *in vivo* application of ^{19}F MRI is limited by its intrinsic low sensitivity, which requires sufficient local ^{19}F concentration for detection. Consistent with this, no detectable tumor signal was observed after intravenous administration of ***Pc*-Mn/Foil@MA**, whereas high-SNR ^{19}F MRI signals were obtained after intratumoral injection (Fig. 5K and L; Fig. S19), demonstrating its *in vivo* imaging capability under sufficient local concentration.

2.5. *In vivo* phototherapy of gliomas with Pc-Mn/Foil@MA

Given its potent *in vitro* phototherapeutic effects, glioma-targeting capability, and BBB penetration, the *in vivo* efficacy of ***Pc*-Mn/Foil@MA** was evaluated in both subcutaneous and orthotopic glioma models. Initial studies were conducted in mice bearing subcutaneous U-87 MG tumors. When tumors reached ~100 mm^3, mice were randomized into six groups and treated every three days via intravenous injection of ***Pc*-Mn/Foil@MA**, ***Pc*-Mn/Foil@SA**, or PBS at 2.5 μmol kg^{-1}, based on the prolonged tumor retention observed by NIRFI (up to 72 h). Subgroups were irradiated with a 660 nm laser (0.35 W cm^{-2}, 10 min) at 24 and 48 h post-injection (Fig. 6A).

Tumor volumes were monitored every two days for 14 days. Minimal tumor inhibition was observed in the PBS, PBS + laser, ***Pc*-Mn/Foil@SA**, and ***Pc*-Mn/Foil@MA** groups, while significant suppression occurred in the ***Pc*-Mn/Foil@SA** + laser and ***Pc*-Mn/Foil@MA** + laser groups (Fig. 6B–H). No significant difference was observed between the two laser-treated groups, suggesting comparable therapeutic efficacy. The ***Pc*-Mn/Foil@MA** + laser group exhibited a tumor growth index (TGI) of 86% (Fig. S20). Consistently, final tumor volume in this group averaged 77 mm^3, compared to 909 mm^3 in the PBS group (Fig. 6I), further confirming the potent therapeutic efficacy.

No significant body weight loss or histopathological abnormalities in major organs were observed (Fig. 6J; Fig. S21). Hepatic and renal function, including alanine aminotransferase (ALT), aspartate aminotransferase (AST), creatinine (CR), and blood urea nitrogen (BUN), remained within normal ranges, indicating no systemic toxicity (Fig. S22). Tumor section staining from ***Pc*-Mn/Foil@SA** + laser and ***Pc*-Mn/Foil@MA** + laser groups exhibited decreased cell density, reduced Ki-67 expression, and increased apoptosis level (Fig. 6K–M). In addition, HIF-1α staining showed reduced expression in nanoemulsion-treated tumors compared with PBS controls (Fig. 6K–N), while pimonidazole

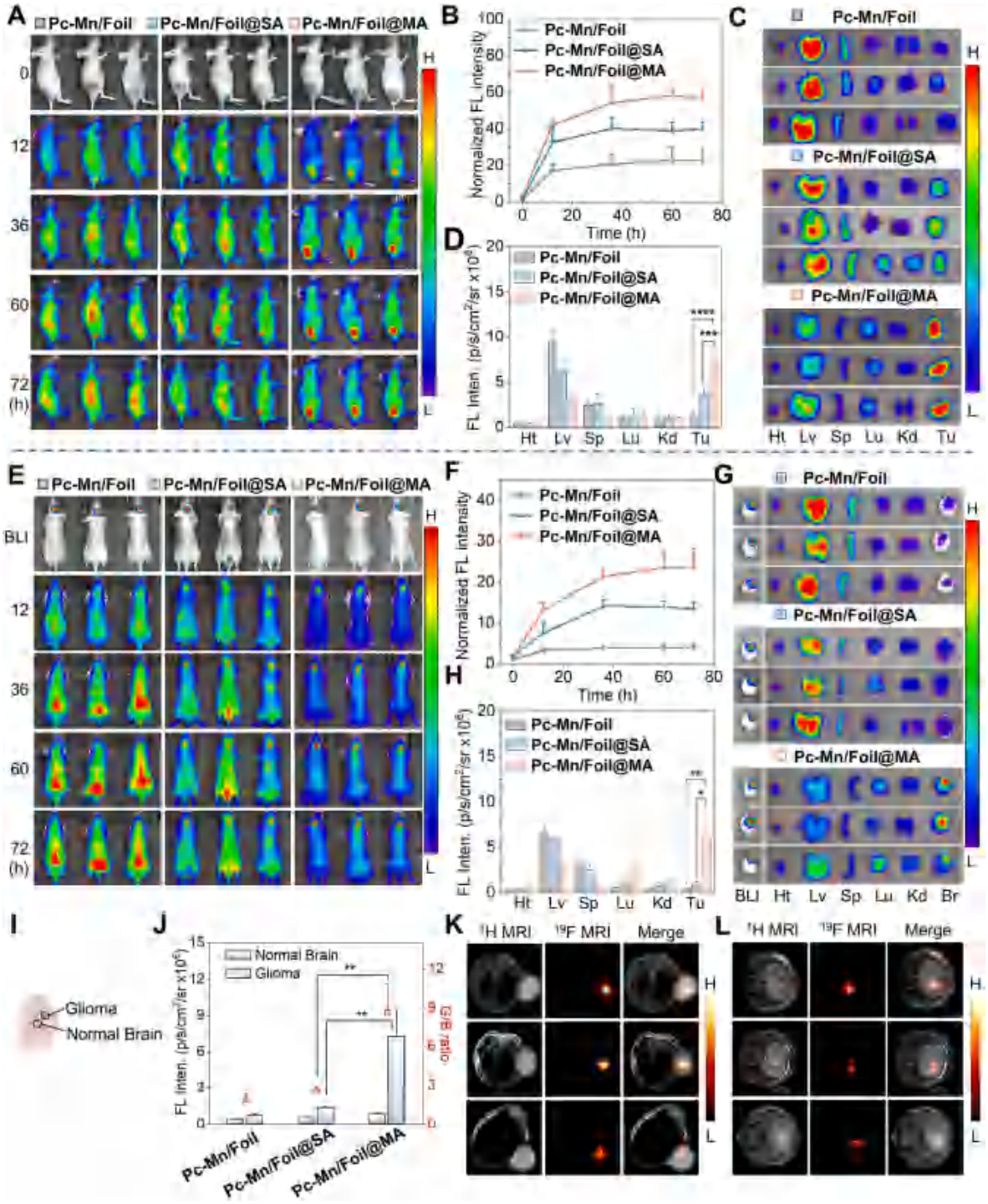

Fig. 5. *In vivo* biodistribution of nanoemulsions in mouse glioma models. Time-dependent NIRFI of mice with subcutaneous tumors (A) and quantitative FL intensities of the tumor regions (B). *Ex vivo* NIRFI (C) and corresponding FL intensities (D) of the internal organs and tumors collected at 72 h post-injection. Time-dependent NIRFI of mice with orthotopic gliomas (E) and corresponding FL intensities of the tumor regions (F). *Ex vivo* NIRFI (G) and corresponding FL intensities (H) of the internal organs and tumors collected at 72 h post-injection. Schematic illustration of the glioblastoma and normal brain regions (I). Quantitative FL intensities of the indicated regions in (G) (J, left) and the glioblastoma-to-normal brain (G/B) ratio (J, right) ^{19}F MRI of ***Pc*-Mn/Foil@MA**-treated mice in subcutaneous (K) and orthotopic (L) models, with T_2-weighted ^{1}H MRI used for anatomical reference. Data are presented as mean ± SD; n = 3, *p < 0.05, **p < 0.01, ***p < 0.001, ****p < 0.0001. (Ht: Heart, Lv: Liver, Sp: Spleen, Lu: Lung, Kd: Kidney, Br: Brain, BLI: Bioluminescence Imaging).

staining further confirmed decreased hypoxic regions (Fig. S23), together providing complementary evidence of tumor hypoxia modulation.

The *in vivo* phototherapy efficacy of ***Pc*-Mn/Foil@MA** was further evaluated in mice bearing orthotopic U-87 MG-Luc gliomas. Tumor establishment was confirmed via bioluminescence imaging and ^{1}H MRI, and mice were randomly assigned to five groups. One group received PBS, while the remaining four were treated with a single intravenous injection of ***Pc*-Mn/Foil@SA** or ***Pc*-Mn/Foil@MA** (2.5 μmol kg^{-1}). Phototherapy groups were subjected to craniotomy to expose the tumor region, followed by 660 nm laser irradiation (0.15 W cm^{-2}, 10 min) delivered via an optical fiber directly to the exposed tumor site at 24 h

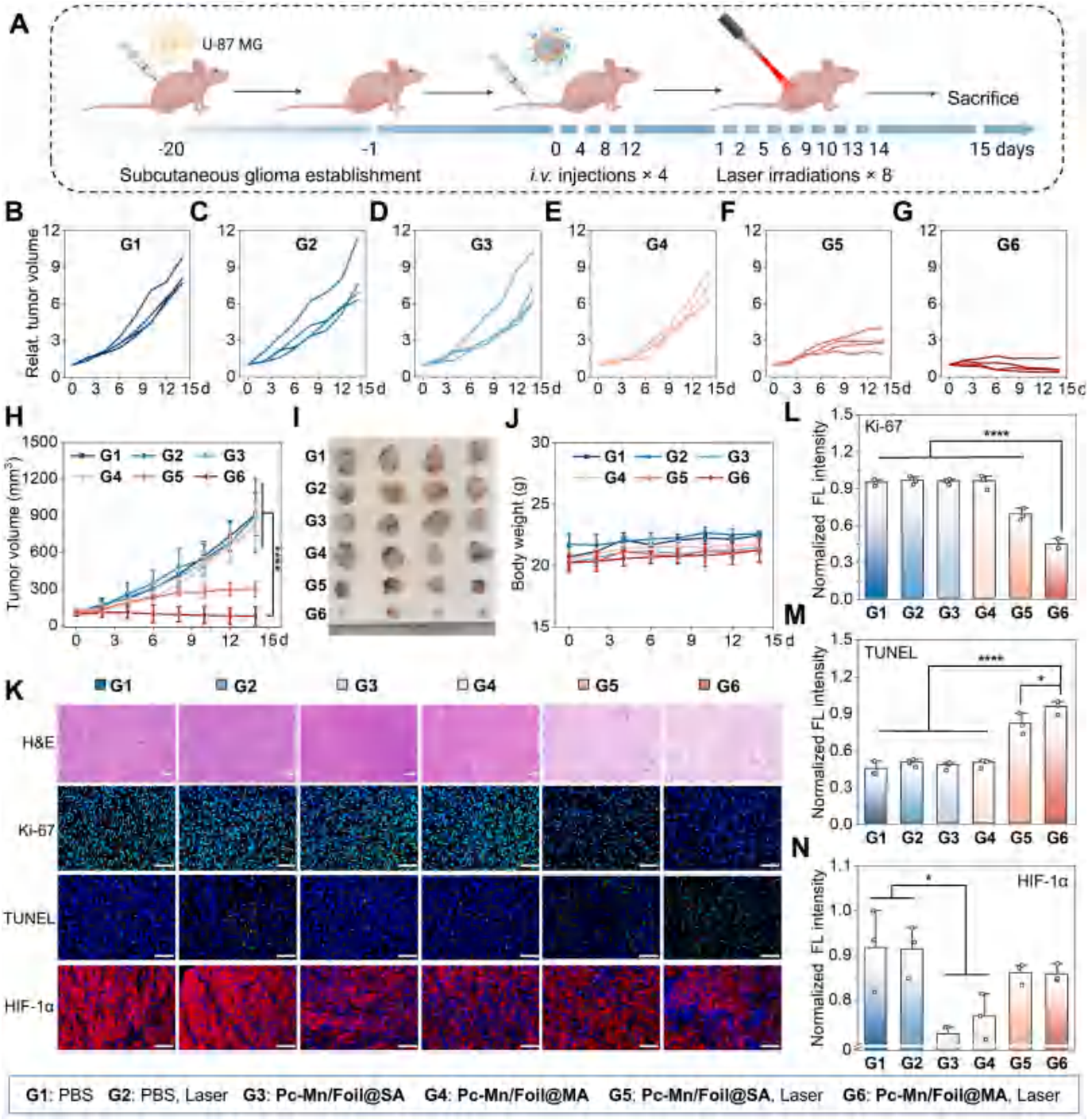

Fig. 6. *In vivo* phototherapy in mice bearing subcutaneous tumors. Schematic of phototherapy schedules (A). Tumor growth curves (B-G: grouped, H: combined), tumor photographs (I), and body weight curves (J) of the treatment group. Representative histological images of tumor tissues, including H&E, Ki-67, TUNEL, and HIF-1α staining (K). Quantitative analysis of Ki-67-positive cells (L), TUNEL-positive cells (M), and HIF-1α-positive cells (N) in tumor tissues. Scale bar is 100 μm for H&E, and 50 μm for Ki-67, TUNEL, and HIF-1α. Data are presented as mean ± SD; n = 4, *p < 0.05, ****p < 0.0001.

post-injection (Fig. 7A), with irradiation limited to a single treatment to minimize potential damage to surrounding normal brain tissue.

Tumor progression was monitored every two days for 10 days using bioluminescence imaging. The lower bioluminescence intensity was observed in both the ***Pc*-Mn/Foil@SA** + laser group and the ***Pc*-Mn/Foil@MA** + laser group compared to the control group, including PBS + laser, ***Pc*-Mn/Foil@SA**, and ***Pc*-Mn/Foil@MA** groups (Fig. 7B; Fig. S24A). These results were corroborated by H&E staining and ^{1}H MRI, which consistently indicated significantly inhibited tumor progression in both laser-treated groups (Fig. 7C and D). Survival analysis revealed significantly prolonged survival in both laser-treated groups, with a median survival of 36 days for ***Pc*-Mn/Foil@MA** + laser versus 27 days for the PBS group (Fig. 7E). No significant difference was observed between the two laser-treated groups, which may be attributed to both achieving sufficient intratumoral photosensitizer levels for effective therapy.

No significant changes in body weight were observed in the ***Pc*-Mn/Foil@SA** and ***Pc*-Mn/Foil@MA** groups (Fig. S24B). H&E staining of

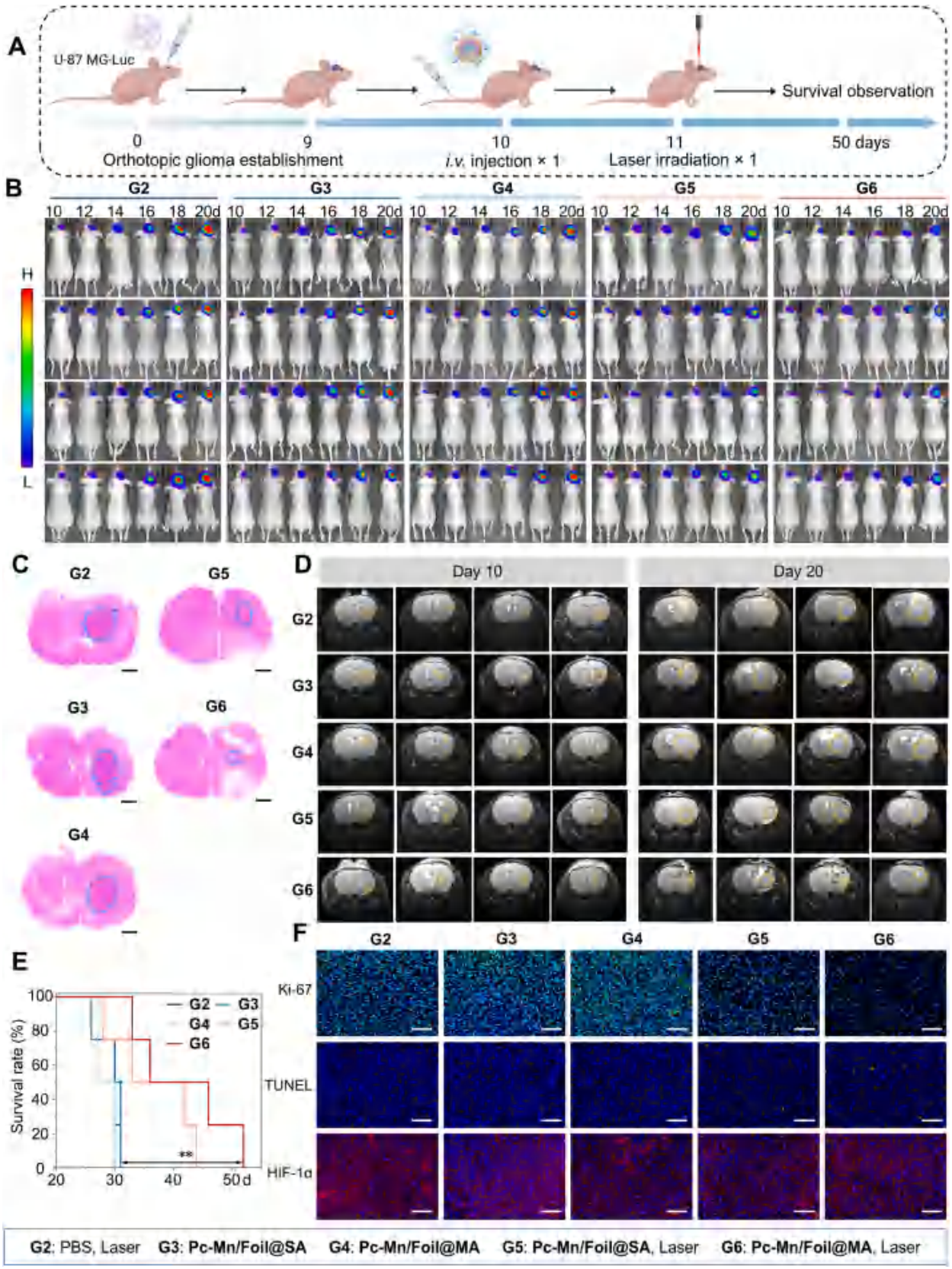

Fig. 7. *In vivo* phototherapy in mice bearing orthotopic tumors. Schematic of phototherapy schedules (A). Bioluminescence images of the treatment groups (B). Representative H&E staining images of *ex vivo* brains harvested from each group on day 20 post-treatment (C). T_2-weighted ^{1}H MRI of the brain region on days 10 and 20 (D). Kaplan-Meier survival curve of mice from different groups (E). Ki-67, TUNEL, and HIF-1α staining of tumor tissues (F). Dashed outlines indicate tumor regions. Scale bar is 1000 μm for H&E and 50 μm for the rest. Data are presented as mean ± SD; n = 4, **p < 0.01.

major organs showed no histological abnormalities (Fig. S25), confirming excellent systemic biocompatibility. Brain tumor sections from ***Pc*-Mn/Foil@MA** + laser-treated mice displayed markedly reduced tumor burden (Fig. 7C). Ki-67 staining indicated decreased proliferation, while TUNEL staining showed the highest apoptosis levels in this group (Fig. 7F; Fig. S26A and B). While reduced hypoxic regions were observed in the subcutaneous model, no statistically significant change in HIF-1α expression was detected in the orthotopic glioma model, despite lower average levels in the ***Pc*-Mn/Foil@SA**- and ***Pc*-Mn/Foil@MA**-treated groups. This discrepancy may be attributed to the more complex microenvironment of orthotopic tumors, including limited perfusion and the presence of the BBB, which can restrict oxygen delivery (Fig. 7F; Fig. S26C).

Collectively, these results demonstrate that ***Pc*-Mn/Foil@MA** enables tumor-specific accumulation, modulates hypoxia, and enhances PDT efficacy, resulting in effective tumor growth inhibition and increased apoptosis, with a favorable biosafety profile and prolonged survival in both subcutaneous and orthotopic models.

3. Conclusion

In summary, we developed a fluorinated amphiphilic phthalocyanine-based nanoemulsion through rational side-chain engineering and hierarchical self-assembly to address key challenges in glioma phototherapy, including limited targeting, poor tumor penetration, hypoxia-induced resistance, and insufficient imaging capabilities. Although phthalocyanine is well-suited for NIRFI and phototherapy, its clinical use has been severely hindered by strong aggregation and low solubility. By tailoring the side-chains and Mn^{2+} chelating, we reduced aggregation, improved water solubility, and enabled dual-modality NIRFI/^{19}F MRI and high phototherapy efficacy, yielding a multifunctional "all-in-one" phthalocyanine. Self-assembly with a fluorinated oil amplified NIRFI by 5-fold and enhanced ^{19}F MRI sensitivity 14-fold, while simultaneously enabling oxygen delivery to mitigate hypoxia and enhance PDT. Surface modification with a folic acid-conjugated, acid-responsive charge-reversal polymer promoted pH-triggered cellular uptake, dual-organelle targeting, and effective induction of both apoptosis and pyroptosis upon light activation. *In vivo*, the nanoemulsion crossed the BBB, selectively accumulated in tumors, inhibited glioma growth in both subcutaneous and orthotopic models, and extended survival without observable systemic toxicity. Compared to previous systems with limited imaging contrast or complex architectures, our nanoplatform demonstrates how side-chain- and metal ion-tuned phthalocyanines, combined with fluorous self-assembly and responsive surface chemistry, can enable complementary dual-modal imaging, effective targeting, and potent therapy. Notably, compared with conventional phthalocyanine-based platforms, our system offers depth-independent ^{19}F MRI with negligible background interference, reduced formulation complexity through amphiphilic self-assembly, and environment-responsive charge-reversal delivery within a single nanoemulsion architecture. This study highlights the potential of rationally designed phthalocyanine nanoemulsions as versatile theranostic agents. Although ^{19}F MRI sensitivity was markedly improved, the inherent detection limit still constrains real-time therapeutic monitoring. Future work should simplify molecular design, increase tumor-localized ^{19}F concentration, and integrate immunomodulatory or multimodal therapies to expand its biomedical applications.

4. Materials and methods

4.1. Materials

Polymer **FA-PEG-NH$_2$** was purchased from ToYongBio Tech. Inc. (Shanghai, China). 1,3-Diphenylisobenzofuran (DPBF) was purchased from Aladdin Biochem. Tech. Co., Ltd. (Shanghai, China). 2,2,6,6-Tetramethyl-4-piperidone hydrochloride (TEMP) was obtained from Dojindo Lab. (Kyoto, Japan). 2′,7′-Dichlorodihydrofluorescein diacetate (DCFH-DA), Mitochondrial Tracing Green (MTG), 1,1′-Dioctadecyl-3,3,3′,3′-tetramethylindocarbocyanine perchlorate (Dil), 4′,6-Diamidino-2-phenylindole (DAPI), Calcein/PI cell viability and cytotoxicity assay kit, and enhanced mitochondrial membrane potential assay kit with JC-1 were obtained from Beyotime Biotech. Co., Ltd. (Shanghai, China). Cell Counting Kit-8 (CCK-8) and Annexin V-FITC apoptosis detection kit were purchased from MeilunBio Co. (Dalian, China).

4.2. Preparation and characterization of nanoemulsion

10 mg of ***Pc*-Mn** and 30 mg of **Foil** were dissolved in 1 mL of dichloromethane (DCM) in a round-bottom flask. The solvent was then evaporated under reduced pressure using a rotary evaporator, leaving a uniform thin film on the flask wall. Subsequently, 500 μL of distilled water was added, and the mixture was sonicated for 10 min to redisperse the thin film, affording a clear green emulsion.

FA-PEG-PLL-MA or **FA-PEG-PLL-SA** (30 mg) was dissolved in 500 μL of deionized water. The resulting solution was slowly added to the preformed emulsion under sonication, and the mixture was further sonicated for 10 min to ensure complete assembly, yielding the final nanoemulsion.

4.3. Reactive oxygen species (ROS) detection

The generation of ROS by the nanoemulsions was evaluated using DPBF and TEMP probes. Briefly, a solution of DPBF in *N*,*N*-dimethylformamide (DMF) was mixed with an aqueous solution of the nanoemulsions to obtain final concentrations of 60 μM DPBF and 1 μM nanoemulsion. Following laser irradiation (660 nm, 0.35 W cm^{-2}), the absorption of DPBF at 410 nm was monitored using a UV-Vis spectrophotometer.

Singlet oxygen ($^1O_2$) generation was further assessed by electron paramagnetic resonance (EPR) spectroscopy. Nanoemulsions diluted in PBS (pH 7.4) were mixed with 100 mM TEMP, irradiated for 1 min, and immediately analyzed by EPR.

4.4. In vitro antitumor studies

Cell viability assay: Cytotoxicity was evaluated using a CCK-8 kit. U-87 MG cells were seeded in 96-well plates at a density of 5×10^3 cells per well and cultured for 24 h. The medium was then replaced with fresh medium containing various concentrations of ***Pc*-Mn/Foil@MA** or ***Pc*-Mn/Foil@SA** under different pH conditions for 24 h. After incubation, cells were washed three times with PBS, exposed to laser irradiation (660 nm, 0.35 W cm^{-2}) for 10 min, and further incubated for 12 h. Subsequently, 10 μL of CCK-8 solution was added to each well, and the cells were incubated for 1 h before measuring the absorbance at 450 nm using a microplate reader.

Live/Dead staining: Cell viability and cytotoxicity in 3D spheroids were assessed using Calcein AM and propidium iodide (PI). U-87 MG spheroids were incubated with ***Pc*-Mn/Foil@MA** or ***Pc*-Mn/Foil@SA** (10 μM) under different pH conditions for 24 h, followed by either laser irradiation (660 nm, 0.35 W cm^{-2}) or maintenance in the dark for 10 min. The spheroids were then stained with Calcein AM/PI working solution and imaged by CLSM. ***Pc*-Mn/Foil@SA** at the same concentration was used as a control.

4.5. In vitro ^{19}F MRI

Phantom experiments of ***Pc*-1** and ***Pc*-2**: The compounds were dissolved in methanol and diluted to fluorine concentrations of 80, 40, 20, 10, 5, and 2.5 mM. The corresponding concentrations of compound ***Pc*-1** were 2.22, 1.11, 0.56, 0.28, 0.14, and 0.07 μM, and for ***Pc*-2** were 1.11, 0.56, 0.28, 0.14, 0.07, and 0.03 μM, respectively. ^{19}F MR images were acquired using the following parameters: TR = 1000 ms, TE = 3.0 ms,

FOV = 30 × 30 mm, matrix size = 32 × 32, RARE factor = 1, NS = 4.

Phantom experiments of nanoemulsion: Phantom samples with varying concentrations of ***Pc*-Mn** in water (80, 40, 20, 10, 5, and 2.5 mM) were prepared. T_1-weighted ^{19}F MR images were acquired with the following parameters: TR = 300 ms, TE = 3 ms, FOV = 20 × 20 mm, matrix size = 32 × 32, RARE factor = 4, NS = 250. Density-weighted ^{19}F MR images were acquired with the following parameters: TR = 1500 ms, TE = 3 ms, FOV = 20 × 20 mm, matrix size = 32 × 32, RARE factor = 4, NS = 64.

Cellular ^{19}F MRI: For the time-dependent uptake study, U-87 MG cells (1×10^6) were seeded and allowed to adhere for 24 h. The cells were then incubated with fresh DMEM (pH 6.4) containing ***Pc*-Mn/Foil@MA** for 12, 24, 36, and 48 h. After incubation, cells were harvested and counted. Cell pellets (approximately 1.5×10^6 cells) were lysed in 400 μL of cell lysis buffer for ^{19}F MRI. For the pH-dependent uptake study, U-87 MG cells (2×10^6) were incubated with ***Pc*-Mn/Foil@MA** or ***Pc*-Mn/Foil@SA** under different pH conditions for 24 h. Cell pellets (approximately 5×10^6 cells) were then transferred to 0.2 mL eppendorf tubes for ^{19}F MRI. All cellular ^{19}F MR images were acquired with: TR = 1500 ms, TE = 3 ms, FOV = 30 × 30 mm^2, matrix size = 32 × 32, RARE factor = 4, NS = 64.

4.6. Biodistribution study

The biodistribution of ***Pc*-Mn/Foil@MA** was evaluated in BALB/c nude mice bearing subcutaneous U-87 MG tumors or orthotopic U-87 MG-Luc tumors (6 weeks old, approximately 20 g, n = 3). ***Pc*-Mn/Foil@MA** was administered via intravenous injection (dose: 2.5 μmol kg^{-1} of ***Pc*-Mn**). *In vivo* fluorescence images were acquired at various time points using a small animal optical imaging system (IVIS) (λ_{ex} = 675 nm, λ_{em} = 740 nm). At 72 h post-injection, the mice were euthanized, and major organs (heart, liver, spleen, lung, and kidney) and tumors were harvested. *Ex vivo* fluorescence imaging was performed, and the fluorescence intensity was quantified. ***Pc*-Mn/Foil** and ***Pc*-Mn/Foil@SA** at the same dose were used as controls.

4.7. In vivo therapeutic assessment

Mice bearing subcutaneous U-87 MG tumors (tumor volumes 80-120 mm^3) were randomly divided into six groups (n = 4): PBS, PBS + laser (L), ***Pc*-Mn/Foil@SA**, ***Pc*-Mn/Foil@MA**, ***Pc*-Mn/Foil@SA** + L, and ***Pc*-Mn/Foil@SA** + L. The corresponding nanoemulsions were administered via intravenous injection every four days (dose: 2.5 μmol kg^{-1} of ***Pc*-Mn**). For the laser groups, tumors were irradiated with a 660 nm laser (0.35 W cm^{-2}) for 10 min at 24 and 48 h post-injection. This cycle of injection and laser irradiation was repeated four times. Tumor length and width were measured every two days using a caliper.

Mice bearing U-87 MG-Luc orthotopic glioblastoma (n = 4) were randomly divided into five groups: PBS + L, ***Pc*-Mn/Foil@SA**, ***Pc*-Mn/Foil@MA**, ***Pc*-Mn/Foil@SA** + L, and ***Pc*-Mn/Foil@MA** + L. On day 10 post-implantation, the corresponding nanoemulsions were intravenously administered to the mice (dose: 2.5 μmol kg^{-1} of ***Pc*-Mn**). At 24 h post-injection, a cranial window was created in the laser groups, and a 1 mm optical fiber was inserted 3 mm deep into the tumor center for 660 nm irradiation (0.15 W cm^{-2}, 10 min). Tumor progression was monitored every two days via bioluminescence imaging (IVIS).

Body weight (both models) and survival (orthotopic model) were recorded throughout the study. At the end of the experiments, major organs, tumors, and brain tissues were harvested for histopathological analysis.

4.8. Statistical analysis

Quantitative data are presented as mean ± standard deviation (mean ± SD) from at least three independent experiments. Statistical analysis was performed using one-way analysis of variance (ANOVA) followed by Tukey's multiple comparison test for comparisons among three or more groups. For comparisons between two groups, an unpaired two-sided Student's t-test was used. Survival analysis was conducted using the Kaplan-Meier method, and differences between survival curves were assessed by the log-rank test. Statistical significance was defined as *p < 0.05, **p < 0.01, ***p < 0.001, ****p < 0.0001.

CRediT authorship contribution statement

Tingjuan Wu: Data curation, Formal analysis, Investigation, Methodology, Validation, Visualization. **Qiao Yu:** Formal analysis, Investigation, Writing – review & editing. **Jing Zhang:** Data curation, Investigation. **Lijun Zhu:** Validation. **Chaohui Ye:** Supervision. **Xin Zhou:** Funding acquisition, Resources, Supervision. **Yu Li:** Data curation, Formal analysis, Writing – review & editing. **Zhong-Xing Jiang:** Conceptualization, Funding acquisition, Supervision, Writing – original draft.

Declaration of competing interest

The authors declare that they have no known competing financial interests or personal relationships that could have appeared to influence the work reported in this paper.

Acknowledgements

This work was supported by the Strategic Priority Research Program of the Strategic Priority Research Program of the Chinese Academy of Sciences, China (XDB0540000) and the National Natural Science Foundation of China (22327901, 82127802).

Appendix. ASupplementary data

Supplementary data to this article can be found online at https://doi.org/10.1016/j.mtbio.2026.103269.

Data availability

Data will be made available on request.

References

[1] M.J. van den Bent, M. Geurts, P.J. French, M. Smits, D. Capper, J.E.C. Bromberg, S. M. Chang, Primary brain tumours in adults, Lancet 402 (10412) (2023) 1564–1579.
[2] M. Weller, P.Y. Wen, S.M. Chang, L. Dirven, M. Lim, M. Monje, G. Reifenberger, Glioma, Nat. Rev. Dis. Primers 10 (1) (2024) 33.
[3] S. Singh, D. Dey, D. Barik, I. Mohapatra, S. Kim, M. Sharma, S. Prasad, P. Wang, A. Singh, G. Singh, Glioblastoma at the crossroads: current understanding and future therapeutic Horizons, Signal Transduct. Targeted Ther. 10 (1) (2025) 213.
[4] T.S. van Solinge, L. Nieland, E.A. Chiocca, M.L.D. Broekman, Advances in local therapy for glioblastoma - taking the fight to the tumour, Nat. Rev. Neurol. 18 (4) (2022) 221–236.
[5] A. Lauko, A. Lo, M.S. Ahluwalia, J.D. Lathia, Cancer cell heterogeneity & plasticity in glioblastoma and brain tumors, Semin. Cancer Biol. 82 (2022) 162–175.
[6] T.T. Lah, M. Novak, B. Breznik, Brain malignancies: glioblastoma and brain metastases, Semin. Cancer Biol. 60 (2020) 262–273.
[7] C.D. Arvanitis, G.B. Ferraro, R.K. Jain, The blood-brain barrier and blood-tumour barrier in brain tumours and metastases, Nat. Rev. Cancer 20 (1) (2020) 26–41.
[8] A.C. Tan, D.M. Ashley, G.Y. López, M. Malinzak, H.S. Friedman, M. Khasraw, Management of glioblastoma: state of the art and future directions, CA Cancer J. Clin. 70 (4) (2020) 299–312.
[9] L. Yi, Z. Zhang, W. Zhou, Y. Zhang, Y. Hu, A. Guo, Y. Cheng, Z. Qian, P. Zhou, X. Gao, BRD4 degradation enhanced glioma sensitivity to temozolomide by regulating Notch1 via Glu-modified GSH-responsive nanoparticles, Adv. Sci. 11 (48) (2024) 2409753.
[10] B. Wang, S. Hu, Y. Teng, J. Chen, H. Wang, Y. Xu, K. Wang, J. Xu, Y. Cheng, X. Gao, Current advance of nanotechnology in diagnosis and treatment for malignant tumors, Signal Transduct. Targeted Ther. 9 (1) (2024) 200.
[11] R. Zhang, S. Zhang, Z. Zhang, Y. Zhang, L. Yi, Y. Cheng, Z. Qian, X. Zan, X. Gao, MCL1 inhibitor augmented the anti-glioma efficacy of paclitaxel utilizing a multifunctional cascade nanodrug system, Adv. Funct. Mater. 35 (5) (2025) 2414499.

[12] H. Huang, S. Che, W. Zhou, Y. Zhang, W. Zhuo, X. Yang, S. Zheng, J. Liu, X. Gao, Apatinib potentiates doxorubicin with cRGD-functionalized pH-sensitive micelles against glioma, Chin. Chem. Lett. 36 (5) (2025) 110084.
[13] Y. Qin, L. Yang, Y. Yang, W. Gao, K. Aihemaiti, G. Jiang, R. Huang, H. Khan, R. Huang, Overcoming multiple barriers to deliver photo-gene system for glioma-targeted combined therapy, J. Contr. Release 376 (2024) 542–552.
[14] W. Zhang, M. Kang, X. Li, Y. Pan, Z. Li, Y. Zhang, C. Liao, G. Xu, Z. Zhang, B. Z. Tang, Z. Xu, D. Wang, Fiber optic-mediated type I photodynamic therapy of brain glioblastoma based on an aggregation-induced emission photosensitizer, Adv. Mater. 36 (47) (2024) e2410142.
[15] G. Li, S. Jiang, Z. Zhang, X. Liu, K. Wu, P. Liu, M. Yang, T. Zhou, J. Xiao, N. Xin, X. Wu, Z. Chen, J. Ding, C. Wu, D. Wei, J. Sun, A. Tong, H. Fan, L. Zhou, Donor substitution engineering of hemicyanine nanoparticles to reprogram the tumor microenvironment and enhance Fn14-targeted bite for glioblastoma photoimmunotherapy, Adv. Funct. Mater. 35 (3) (2025) 2413847.
[16] L. Liu, J. Zhang, R. An, Q. Xue, X. Cheng, Y. Hu, Z. Huang, L. Wu, W. Zeng, Y. Miao, J. Li, Y. Zhou, H.Y. Chen, H. Liu, D. Ye, Smart nanosensitizers for activatable sono-photodynamic immunotherapy of tumors by redox-controlled disassembly, Angew. Chem., Int. Ed. 62 (10) (2023) e202217055.
[17] Y. Cai, T. Chai, W. Nguyen, J. Liu, E. Xiao, X. Ran, Y. Ran, D. Du, W. Chen, X. Chen, Phototherapy in cancer treatment: strategies and challenges, Signal Transduct. Targeted Ther. 10 (1) (2025) 115.
[18] Y. Wang, K. Ma, M. Kang, D. Yan, N. Niu, S. Yan, P. Sun, L. Zhang, L. Sun, D. Wang, H. Tan, B.Z. Tang, A new era of cancer phototherapy: mechanisms and applications, Chem. Soc. Rev. 53 (24) (2024) 12014–12042.
[19] P. Chen, Y. Liu, H. Huang, M. Li, H. Xie, S. Roy, J. Gu, J. Jin, K. Deng, L. Du, B. Guo, Genetically engineered IL12/CSF1R-macrophage membrane-liposome hybrid nanovesicles for NIR-II fluorescence imaging-guided and membrane-targeted mild photothermal-immunotherapy of glioblastoma, Adv. Sci. 12 (23) (2025) 2500131.
[20] H. Baghirov, Receptor-mediated transcytosis of macromolecules across the blood-brain barrier, Expert Opin. Drug Deliv. 20 (12) (2023) 1699–1711.
[21] L. Han, C. Jiang, Evolution of blood-brain barrier in brain diseases and related systemic nanoscale brain-targeting drug delivery strategies, Acta Pharm. Sin. B 11 (8) (2021) 2306–2325.
[22] M.D. Caverzán, P.M. Oliveda, L. Beaugé, R.E. Palacios, C.A. Chesta, L.E. Ibarra, Metronomic photodynamic therapy with conjugated polymer nanoparticles in glioblastoma tumor microenvironment, Cells 12 (11) (2023) 1541.
[23] W.S. Kim, M.I. Khot, H.M. Woo, S. Hong, D.H. Baek, T. Maisey, B. Daniels, P. L. Coletta, B.J. Yoon, D.G. Jayne, S.I. Park, AI-enabled, implantable, multichannel wireless telemetry for photodynamic therapy, Nat. Commun. 13 (1) (2022) 2178.
[24] Y. Yang, Q. Jiang, F. Zhang, Nanocrystals for deep-tissue in vivo luminescence imaging in the near-infrared region, Chem. Rev. 124 (2) (2024) 554–628.
[25] H. Wang, X. Mu, J. Yang, Y. Liang, X.-D. Zhang, D. Ming, Brain imaging with near-infrared fluorophores, Coord. Chem. Rev. 380 (2019) 550–571.
[26] X. Wu, Y. Deng, R. Wang, H. Kim, G. Kim, Y. Xu, K.T. Hong, J.-S. Lee, J.-J. Hu, G. Liang, J. Yoon, Rational design of an activatable near-infrared fluorogenic platform for in vivo orthotopic tumor imaging and resection, Angew. Chem., Int. Ed. 64 (4) (2025) e202416877.
[27] J. Wang, Y. Liu, C. Qi, Z. Luo, J. Wei, G. Wang, M. Ismail, Y. Zhong, B. Shi, Near-infrared theranostics for brain diseases: design, engineering, and emerging applications, Coord. Chem. Rev. 534 (2025) 216591.
[28] D. Chen, J. Guo, A. Li, C. Sun, H. Lin, H. Lin, C. Yang, W. Wang, J. Gao, Metabolic fluorine labeling and hotspot imaging of dynamic gut microbiota in mice, Sci. Adv. 9 (4) (2023) eabg6808.
[29] E.T. Ahrens, R. Flores, H. Xu, P.A. Morel, In vivo imaging platform for tracking immunotherapeutic cells, Nat. Biotechnol. 23 (8) (2005) 983–987.
[30] I. Tirotta, V. Dichiarante, C. Pigliacelli, G. Cavallo, G. Terraneo, F.B. Bombelli, P. Metrangolo, G. Resnati, ^{19}F magnetic resonance imaging (MRI): from design of materials to clinical applications, Chem. Rev. 115 (2) (2015) 1106–1129.
[31] H. Zhang, Q. Yu, Y. Li, Z. Yang, X. Zhou, S. Chen, Z.-X. Jiang, Fluorinated cryptophane-A and porphyrin-based theranostics for multimodal imaging-guided photodynamic therapy, Chem. Commun. 56 (25) (2020) 3617–3620.
[32] L. Yang, F. Wang, Y. Li, R. Zhou, A.F. Li, T.J. Wu, M.S. Qiu, L. Zhang, M.H. Yang, X. Zhou, Z.-X. Jiang, S.Z. Chen, Mechanical interlocking of 144 symmetrical ^{19}F and tetraphenylethylene for magnetic resonance-fluorescence dual imaging, J. Am. Chem. Soc. 147 (8) (2025) 7137–7147.
[33] A.F. Li, F. Wang, Y. Li, X.X. Peng, Y.Q. Liu, L.J. Zhu, P. He, T.T. Yu, D.Q. Chen, M. J. Duan, X. Zhou, Z.-X. Jiang, S.Z. Chen, Fluorination of aza-BODIPY for cancer cell plasma membrane-targeted imaging and therapy, ACS Appl. Mater. Interfaces 17 (2) (2025) 3013–3025.
[34] Y.J. Zheng, L.J. Zhu, C.S. Ke, Y. Li, Z.W. Zhou, M. Jiang, F. Wang, P. He, X. Zhou, Z.-X. Jiang, S.Z. Chen, Fluorinated macromolecular amphiphiles as prototypic molecular drones, Proc. Natl. Acad. Sci. USA 121 (35) (2024) e2405877121.
[35] Z. Liang, Y. Yang, F. Jia, K. Sai, S. Ullah, C. Fidelis, Z. Lin, F. Li, Intrathecal delivery of folate conjugated near-infrared quantum dots for targeted in vivo imaging of gliomas in mice brains, ACS Appl. Bio Mater. 2 (4) (2019) 1432–1439.
[36] M. Song, J. Tian, L. Wang, S. Dong, K. Fu, S. Chen, C. Liu, Efficient delivery of lomitapide using hybrid membrane-coated tetrahedral DNA nanostructures for glioblastoma therapy, Adv. Mater. 36 (24) (2024) e2311760.
[37] W. Huang, L. Zhang, J. Sun, Y. Sun, L. Gong, S. Ge, Y. Zheng, W. Gao, X. Wei, Hypoxia reversion by low-immunogenic ultra-acid-sensitive comicelles of protein-polymer conjugates sensitizes tumors to photodynamic therapy, J. Am. Chem. Soc. 146 (11) (2024) 7543–7554.
[38] D.T. Nguyen, M.J. Baek, S.M. Lee, D. Kim, S.Y. Yoo, J.Y. Lee, D.D. Kim, Photobleaching-mediated charge-convertible cyclodextrin nanoparticles achieve deep tumour penetration for rectal cancer theranostics, Nat. Nanotechnol. 19 (11) (2024) 1723–1734.
[39] Z. Zhao, K. He, B. Liu, W. Nie, X. Luo, J. Liu, Intrarenal pH-responsive self-assembly of luminescent gold nanoparticles for diagnosis of early kidney injury, Angew. Chem., Int. Ed. 63 (29) (2024) e202406016.
[40] J. Jägers, A. Wrobeln, K.B. Ferenz, Perfluorocarbon-based oxygen carriers: from physics to physiology, Pflugers Arch. – Eur. J. Physiol. 473 (2) (2021) 139–150.
[41] H. Wang, J. Li, Y. Wang, X. Gong, X. Xu, J. Wang, Y. Li, X. Sha, Z. Zhang, Nanoparticles-mediated reoxygenation strategy relieves tumor hypoxia for enhanced cancer therapy, J. Contr. Release 319 (2020) 25–45.
[42] Y. Cheng, H. Cheng, C. Jiang, X. Qiu, K. Wang, W. Huan, A. Yuan, J. Wu, Y. Hu, Perfluorocarbon nanoparticles enhance reactive oxygen levels and tumour growth inhibition in photodynamic therapy, Nat. Commun. 6 (1) (2015) 8785.
[43] X. Liang, M. Chen, P. Bhattarai, S. Hameed, Z. Dai, Perfluorocarbon@porphyrin nanoparticles for tumor hypoxia relief to enhance photodynamic therapy against liver metastasis of colon cancer, ACS Nano 14 (10) (2020) 13569–13583.
[44] H. Wang, Y. Guo, C. Wang, X. Jiang, H. Liu, A. Yuan, J. Yan, Y. Hu, J. Wu, Light-controlled oxygen production and collection for sustainable photodynamic therapy in tumor hypoxia, Biomaterials 269 (2021) 120621.
[45] Y.-Y. Zhao, Y. Xu, X. Zhang, Z. Chen, H. Kim, X. Li, J. Yoon, A hypoxia-triggered bioreduction of hydrophilic type I photosensitizer for switchable in vivo photoacoustic imaging and high-specificity cancer phototherapy, Angew. Chem., Int. Ed. 64 (25) (2025) e202506412.
[46] G.T. Nash, T. Luo, G. Lan, K. Ni, M. Kaufmann, W. Lin, Nanoscale metal-organic layer isolates phthalocyanines for efficient mitochondria-targeted photodynamic therapy, J. Am. Chem. Soc. 143 (5) (2021) 2194–2199.
[47] R. Li, Y. Zhou, Y. Liu, X. Jiang, W. Zeng, Z. Gong, G. Zheng, D. Sun, Z. Dai, Asymmetric, amphiphilic RGD conjugated phthalocyanine for targeted photodynamic therapy of triple negative breast cancer, Signal Transduct. Targeted Ther. 7 (1) (2022) 64.
[48] M. Srinivas, A. Heerschap, E.T. Ahrens, C.G. Figdor, I.J.M. de Vries, ^{19}F MRI for quantitative in vivo cell tracking, Trends Biotechnol. 28 (7) (2010) 363–370.
[49] E.T. Ahrens, J.W.M. Bulte, Tracking immune cells in vivo using magnetic resonance imaging, Nat. Rev. Immunol. 13 (10) (2013) 755–763.
[50] X. Peng, Y. Li, L. Zhu, X. Zhou, S. Chen, Z.X. Jiang, Enabling ^{19}F MRI and boosting phototherapy through facile counterion pairing of photosensitizers, Small 35 (21) (2025) e2505497.
[51] Y. Chen, T. Xiong, M. Gu, M. Li, X. Chen, L. Wang, J. Fan, X. Peng, Pyrazolone-modified photosensitizers for precise cell membrane rupture to enhance cancer immunotherapy, J. Am. Chem. Soc. 147 (21) (2025) 17915–17925.
[52] Y. Xu, D. An, T. Zhang, X. Wu, S. Wang, J. Shao, L.L. Qu, Y. Guo, X. Dong, Mitochondrion-targeted type I photodynamic therapy for agonist independent cGAS-STING activation, Adv. Mater. 37 (14) (2025) e2418894.
[53] J. Zhuang, Z. Ma, N. Li, H. Chen, L. Yang, Y. Lu, K. Guo, N. Zhao, B.Z. Tang, Molecular engineering of plasma membrane and mitochondria dual-targeted NIR-II AIE photosensitizer evoking synergetic pyroptosis and apoptosis, Adv. Mater. 36 (5) (2024) e2309488.